International Forum on Aeroelasticity and Structural Dynamics
IFASD 2019
9-13 June 2019, Savannah, Georgia, USA

LINEARIZED NAVIER-STOKES CFD FLUTTER CORRELATIONS WITH WIND TUNNEL MEASUREMENTS ON A TRANSONIC U-TAIL FLUTTER MOCK-UP

Hadrien Mamelle[1], Gabriel Broux[1], Nicolas Forestier[1], Zdenek Johan[1], and Eric Garrigues[1]

[1] Dassault Aviation
78 quai Marcel Dassault, 92552 Saint-Cloud France
hadrien.mamelle@dassault-aviation.com

Keywords: flutter, transonic, wind tunnel, CFD, linearized Navier-Stokes, unsteady.

Abstract: Innovative aircraft configurations comprising intersecting surfaces like U-tails exhibit aerodynamic phenomena which are computationally challenging to predict in view of flutter behavior assessment. From the subsonic domain, where aerodynamic interactions occur between the tail surfaces, to the transonic domain, where shock waves and separated flow at the tails intersection increase significantly the flow field complexity, it is necessary to validate not only aerodynamic models but also the aeroelastic coupling strategy involved in flutter computations. To this aim, a comprehensive experimental database has been acquired for several U-tail configurations in subsonic and transonic domains on a heavily instrumented wind tunnel flutter mock-up. This article presents aerodynamic and flutter correlations between experimental and numerical results which are computed with an in-house linearized Navier-Stokes solver with linearized turbulence. The overall strategy set up to obtain these correlations is discussed in detail to highlight the rigorousness required at every stage of the process to be able to compare properly normalized experimental data with adequate numerical data. Starting from accurate steady pressure field predictions in subsonic and transonic domains, unsteady pressure sensitivities induced by a pitching motion are analyzed and point out that linearized Navier-Stokes results are in very good agreement with the measured data, including in the corner area at the tails intersection. A tuned FEM modal basis representative of the mock-up dynamic behavior is used to compute a linearized pressure database which is used to perform frequency-domain flutter computations. The computed flutter diagrams and the predicted flutter pressure variation with respect to the Mach number are in excellent agreement with the measured ones. Thanks to the availability of flutter onsets measurements, flutter mode shape and pressure have been extracted and offer an uncommon opportunity to perform correlations at the flutter point. The predicted bending/torsion flutter mechanism is identical to the measured one and good flutter mode pressure correlations are obtained, providing an additional way to validate aerodynamic predictions. The flutter mode pressure is further analyzed by separating the contributions from the real and imaginary parts of the flutter mode shape to get a deeper understanding of the measured data. Altogether, the results presented in this article constitute a milestone toward numerical tools validation and demonstrate the relevance of the computational strategy adopted at Dassault Aviation in performing accurate aerodynamic and flutter predictions for intersecting surfaces configurations.

1 INTRODUCTION

The design of innovative aircraft configurations like the U-tail depicted in Figure 1 raises several challenges. Indeed the flutter behavior of such empennage configuration is significantly influenced by specific aerodynamic phenomena which are computationally challenging to predict. As the U-shape consists of a vertical tail intersecting a horizontal tail, a first challenge is to predict accurately the aerodynamic interactions between the tail surfaces. These interactions have a direct impact on structural loads and flutter, and thus on the configuration performance. Additionally, corner flow aspects intervene at the tails intersection and constitute another challenge since highly complex aerodynamic phenomena can arise between the tails boundary layers, shock waves and separated flow. These phenomena also have an influence on structural loads and flutter and, moreover, accurate prediction of separated flow onset is of primary importance for aircraft performances regarding drag issues. Consequently, before envisaging such innovative configurations in a new aircraft development program, reliable aerodynamic and flutter predictions should be available to perform parametric studies in view of optimizing and substantiating these novel configurations. As outlined in Figure 1, ensuring the capability to predict accurately these aerodynamic and flutter phenomena implies to pin down the numerical tools validity domains thanks to dedicated demonstration tests. Hence a modular flutter mock-up has been designed, manufactured and tested in November 2016 in ONERA S2MA pressurized wind tunnel to gather reference experimental data in subsonic and transonic domains.

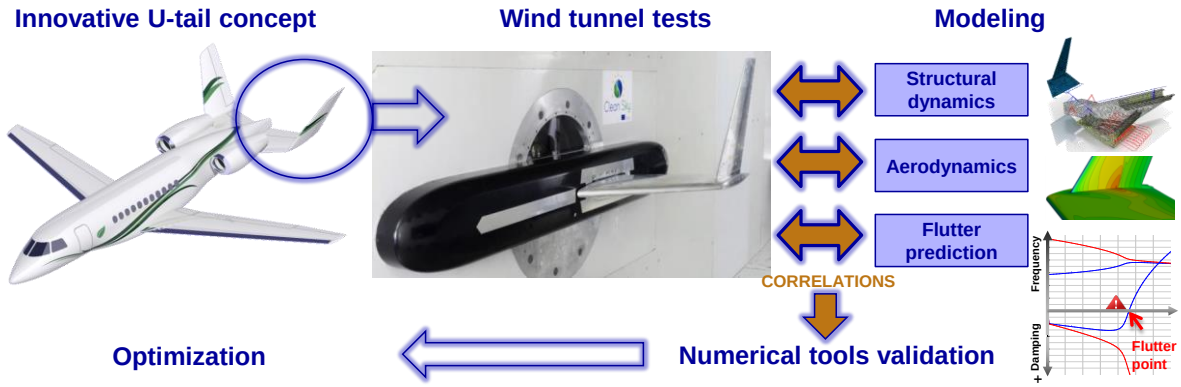

Figure 1: Wind tunnel tests of a U-tail for numerical tools validation.

The mock-up is wall-mounted in the wind tunnel and consists of a fixed dummy fuselage and a half U-tail which external shape is representative of a business jet aft body with a scale factor of 1/8. The model is heavily instrumented and comprises more than 250 unsteady pressure sensors, many accelerometers and some strain gauges for mock-up monitoring. The main features of the mock-up are shown in Figure 2 and an in-depth description of the design and wind tunnel tests is available in [1]. Thanks to the mock-up modularity, several geometrical tail configurations including yaw and dihedral variations have been tested in two main mechanical settings named “pressure” and “flutter” configurations. The pressure configuration is flutter-free and the hydraulic actuator is connected to the shaft to apply harmonic pitching oscillations to the tail. Steady and unsteady pressure data have been measured during these pressure tests for several Mach numbers and frequencies. In the flutter configuration the dynamic behavior is governed by local roll and pitch stiffnesses adjusted to observe flutter inside the wind tunnel test range while the actuator is disconnected from the shaft and used to excite the mock-up. The studied flutter mechanism is a two degrees of freedom flutter involving the first bending and torsion modes of the mock-up and the physics involved in this mechanism is similar to the one identified on a U-Tail aircraft HTP

(Horizontal Tail Plane) flutter. Flutter curves have been measured for several Mach numbers up to the flutter point thanks to an efficient and reliable safety system which allowed exploring the flutter boundary many times without structural damage.

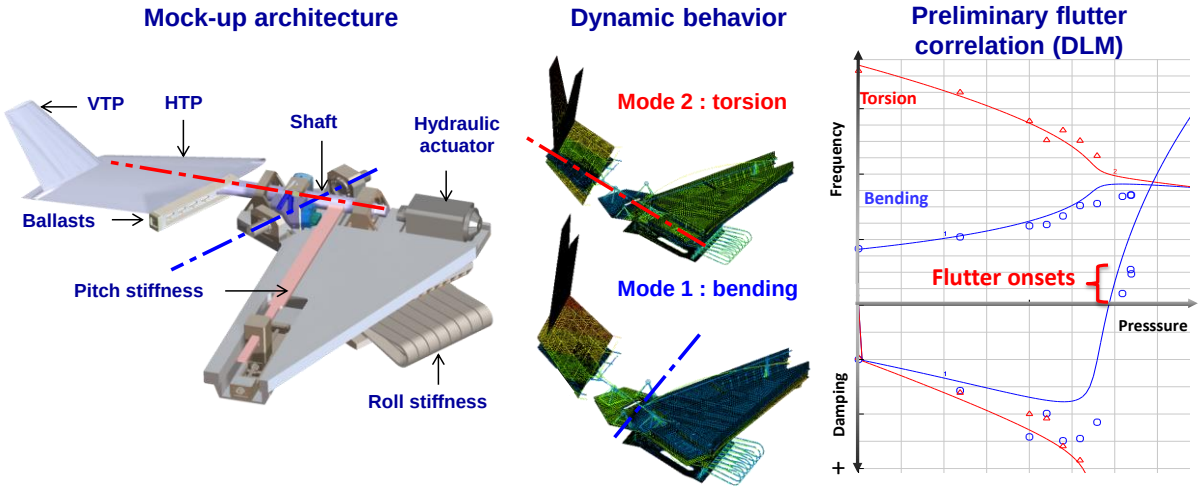

Figure 2: Mock-up architecture, modes involved in flutter mechanism and preliminary flutter curves correlation.

Experimental data processing and analysis as well as preliminary flutter correlations based on DLM (right hand side of Figure 2) have already been presented in 2017 in the proceedings of Come IFASD congress [2]. Following on from these promising results, this article presents advanced numerical investigations carried out in subsonic and transonic domains with a Dassault Aviation in-house linearized Navier-Stokes solver. Theoretical aspects are covered in the first part. The path leading to successful comparisons between experimental and numerical results is presented in a detailed roadmap. Experimental data normalization issue is addressed and a methodology to compare the computed flutter mode pressure field with the measured one is described, enabling to perform unusual pressure correlations using flutter onset data. Pressure and flutter correlations are presented in the two subsequent parts for a tail configuration without dihedral. Harmonic pressure correlations are presented for two frequencies and excellent comparisons are obtained for all Mach numbers. Computed flutter diagrams are then compared to the measured ones and a very good agreement is observed for the frequency and damping variations of the two modes involved in the flutter mechanism. Flutter mode pressure comparisons confirm that the computed flutter mode and the linearized Navier-Stokes predictions yield remarkably good correlations. The analysis is pushed one step further by analyzing the pressure contributions of the real and imaginary parts of the computed flutter mode shape, allowing for an even deeper understanding of the flutter mode pressure profiles. Altogether, these results constitute a milestone toward the numerical tools validation. They prove not only that the quality of the experimental database is appropriate for model validation but also demonstrate that the computational strategy set up at Dassault Aviation to perform aerodynamic and flutter predictions on innovative configurations comprising intersected surfaces is relevant.

2 THEORY & METHODS

A detailed insight of the overall process leading to experimental and numerical correlations is described in this section. Experimental data normalization issues are tackled and flutter mode pressure extraction from flutter onset data is presented. Then the computational strategy set up to obtain numerical results comparable to the experimental ones is presented.

2.1 Roadmap for experimental and numerical correlations

Correlating numerical results with experimental data is a challenging task requiring many kinds of calculations to obtain comparable data. Indeed, the measured data may be post processed in a specific way and the encountered experimental conditions must be accounted for in the computation of numerical results. These considerations lead to the roadmap schematized in Figure 3 where it can be seen that raw data (grey boxes) post processing yields experimental results (green boxes) that can be either compared to numerical results (blue boxes) or used as input in the computations. This roadmap is an enriched version of the one presented in [2] and only new features are discussed in this article. In particular structural correlations are not presented, however it is worth mentioning that the FEM has been tuned with ground vibration tests data and its dynamic behavior is highly representative of the one of the mock-up in the flutter configuration.

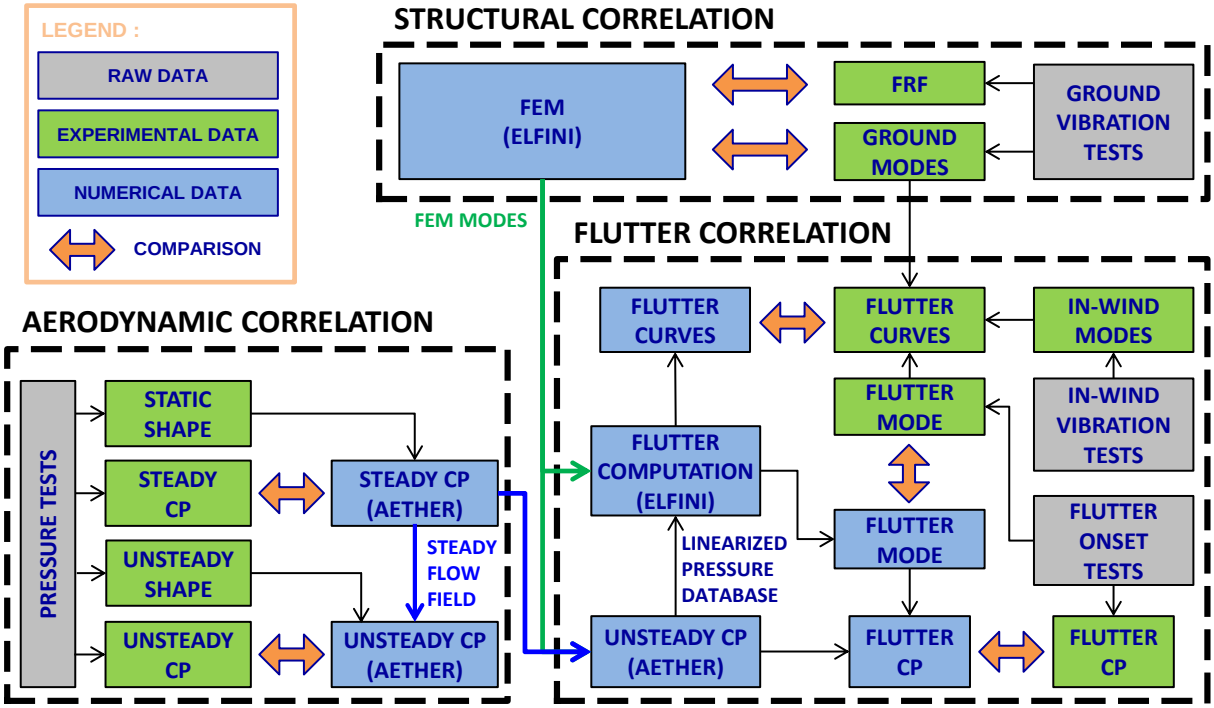

Figure 3: Roadmap for experimental and numerical correlations.

Aerodynamic correlations are performed in a two-step process where the steady pressure field is analyzed before moving to the analysis of the unsteady pressure field. Steady pressure tests give access to steady CP (Pressure Coefficients) and to the associated mock-up static shape which is recorded thanks to MDM data (Model Deformation Measurement). AETHER in-house CFD solver [3] is used to compute the steady flow field and a static shape reconstructed from MDM data can be provided as input to account for the mock-up static deflections. Unsteady pressure tests give access to the pressure sensitivities induced by an imposed pitching motion which is measured thanks to accelerometers. Linearized Navier-Stokes computations [3] are performed either on the theoretical pitch shape or on a reconstructed pitch shape deduced from the unsteady shape measurements. A good correlation on the steady pressure field should be obtained prior any linearized unsteady pressure computation. Indeed, linearized aerodynamic models need to be fed with a reliable steady state pressure field since the linearization is made around a given steady state. Pressure data post-processing is presented in section 2.2.1, information about CFD computations is mentioned in 2.3.1 and aerodynamic correlations are presented in part 3.

Once satisfactory aerodynamic correlations are obtained, it is worth turning to the flutter correlation task which is the most difficult as it involves structural and aerodynamic coupling. Using FEM mode shapes as input, a linear pressure database is generated with AETHER solver and flutter computations based on the p-k method are performed in the frequency domain with ELFINI in-house aeroelastic solver [4, 5]. It is interesting to point out that, apart from the potential use of MDM data in the steady pressure field estimation, only a theoretical FEM modal basis is used to first generate a linearized pressure database and then to perform flutter computations. This strategy avoids the delicate work of shape reconstruction in which noise in the measured ground modal shapes should be cancelled out by an appropriate curve fit procedure and in which lack of spatial information requires adequate shape extrapolation. Flutter tests are used to build flutter curves [2] and flutter onsets give access to the flutter mode shape and its associated pressure field. Flutter data extraction from flutter onset measurements and flutter computation post-processing are explained in sections 2.2.2 and 2.3.2 respectively. All the flutter correlations mentioned in the roadmap depicted in Figure 3 are presented in part 4.

2.2 Experimental data post-processing

Experimental data post-processing is presented below with focus on unsteady pressure data normalization and flutter data extraction from flutter onset measurements. The main objective is to show how to get experimental results that can be readily compared to numerical results.

2.2.1 Pressure test data normalization

Pressure test data normalization drives the way CFD computations should be performed in order to get numerical results that can be readily compared to the measured ones and appropriate data normalization can greatly simplify these computations. During unsteady pressure tests, a harmonic pitching motion is applied to the U-tail by imposing forced oscillations at a fixed frequency ω thanks to the hydraulic actuator which is connected to the shaft. First harmonic extraction technique is used to get the complex amplitudes $H_{raw}(\omega)$ of unsteady raw data comprising mainly pressure and acceleration data. Complex pressure coefficients are delivered together with an unsteady shape which can be used as input for CFD computations. However, computations are facilitated if it is possible to normalize the unsteady data so that the unsteady shape is a real shape (no imaginary part) and they are further simplified if the unsteady shape is known analytically since it avoids the tedious work of delivering a reconstructed shape from the accelerometer data. Consequently unsteady data normalization is not as straightforward as it may seem if complex pressure coefficients associated to a real analytical shape is wanted since it requires determining the suited reference phase ensuring a real shape, the analytical shape representative of the measured shape, and the reference amplitude of this shape.

A dedicated angular sensor was used to measure the rotation of the shaft angle and was thought to be an ideal candidate to normalize the data. Indeed, dividing $H_{raw}(\omega)$ by the complex amplitude of this angular sensor should give a real pitch shape normalized to 1 degree amplitude around the shaft axis. Figure 4 shows the real part (left plot) and imaginary part (right plot) of the complex HTP normal displacements Z_{HTP} normalized with respect to the angular sensor and the corresponding real and imaginary shapes are overlaid to get a practical view of the obtained shapes. Displacements (circle markers) are plotted against their X location and it appears that the imaginary part is non negligible and looks like a pitching motion. Furthermore, due to potential dynamic response of the mock-up, there is no guarantee

that the applied pitching motion corresponds to the theoretical one, namely a pitching motion around the shaft axis. Hence, the angular sensor normalization is not appropriate.

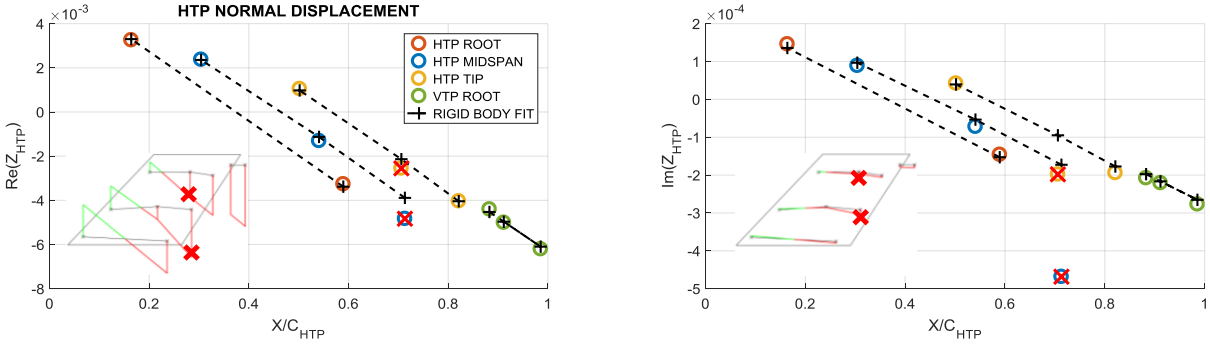

Figure 4: Complex pitch shape obtained with angular sensor normalization.

As the tail parts are stiff and as the imposed pitching motion is a rigid body rotation, a rigid body normalization process has been set up. The analytical normal displacement Z_{theo} of a given accelerometer sensor located on the HTP (X_{acc}, Y_{acc}) due to a rotation around the shaft axis writes as in the upper equation (1), where Λ is the shaft axis angle with respect to the spanwise direction and $(X_{shaft}, Y_{HTP\,root})$ is the point where the shaft axis crosses the HTP root. This equation can be rewritten in a form suitable for curve fitting as shown in the lower equation (1) where the first term is a pitching motion around the spanwise direction (Y axis), the second term is a rolling motion around the chordwise direction (X axis) and the constant term generates plunge. The coefficients a, b and c are obtained thanks to a least squares curve fit of the complex amplitudes Z_{HTP} of the HTP normal displacements.

$$Z_{theo} = -\cos(\Lambda)\cdot X_{acc} + \sin(\Lambda)\cdot Y_{acc} + \cos(\Lambda)\cdot X_{shaft} - \sin(\Lambda)\cdot Y_{HTP\,root}$$
$$Z_{HTP} = -a\cdot X_{acc} + b\cdot Y_{acc} + c \qquad (1)$$

Rigid body curve fit results are shown in Figure 4 where a very good fit is obtained for both the real and imaginary parts (black crosses linked with dotted lines), except for two sensors which obviously suffer from measurement issues (red crosses). Using the phase of the complex coefficient a as the reference phase yields the real pitch shape depicted in Figure 5.

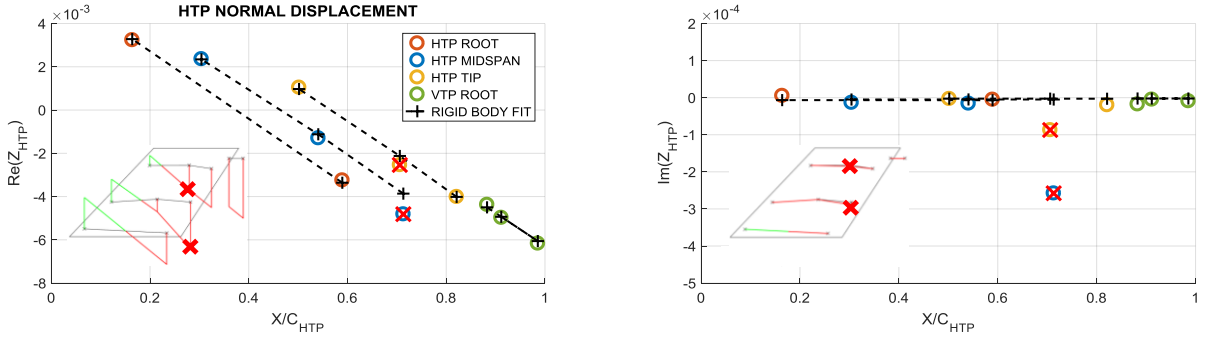

Figure 5: Real pitch shape obtained with rigid body normalization.

The last issue is to determine the analytical shape representative of the applied pitching motion and to enforce its amplitude to be 1° around the applied pitch axis. The formulas allowing to retrieve the applied pitch axis angle Λ_{pitch} and location $(X_{pitch}, Y_{HTP\,root})$ from the rigid body curve fit coefficients are given in equations (2). Finally, the rigid body normalization writes as simply as in equation (3), where a is the complex coefficient obtained

from the rigid body curve fit (1) and H_{norm} is the desired normalized data. The first factor applied to H_{raw} ensures a reference phase based on the pitching motion with 1 radian amplitude around the applied pitch axis while the last factor enforces the amplitude to be 1°.

$$\Lambda_{pitch} = \tan^{-1}\left(\frac{Re[be^{-i\varphi_a}]}{Re[ae^{-i\varphi_a}]}\right) \quad X_{pitch} = tan(\Lambda_{pitch}) \cdot Y_{HTP\ root} \tag{2}$$

$$H_{norm}(\omega) = H_{raw}(\omega) \cdot \frac{\cos(\Lambda_{pitch})}{a} \cdot \frac{\pi}{180} \tag{3}$$

The rigid body normalization has been applied systematically on the unsteady pressure data and ensures that the measured data correspond to a rotation angle of 1° around the applied pitch axis which can be accurately calculated. The applied pitch shape can thus be compared to the theoretical pitch shape as done in 3.3. The least squares curve fit procedure has the advantage of canceling out the noise yielding a reliable reference phase which is of the utmost importance as illustrated in section 3.2.

2.2.2 Flutter data extraction from flutter onset measurements

Flutter data post-processing has already been extensively described in [2], nevertheless some improvements in the flutter onset data post-processing has been done in order to retrieve more reliable flutter mode shape and pressure data from flutter onset measurements. It is important to remind that these measurements are infrequent and difficult to obtain due to the diverging nature of the flutter phenomenon which has damaged many flutter mock-ups in the past and continues to do so. Hence, measuring several flutter onset data is a real feat achieved thanks to rigorous structural design constraints and thanks to an efficient and reliable safety system.

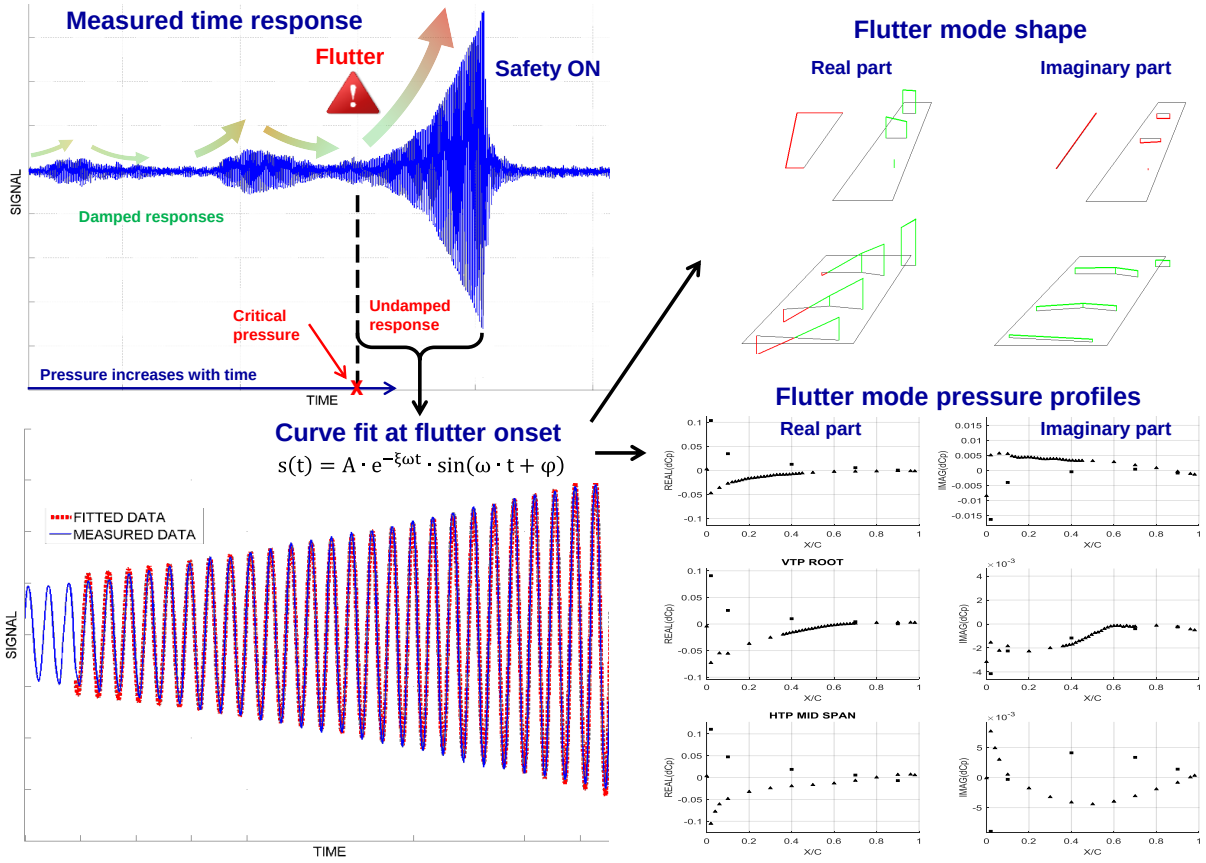

Figure 6: Flutter data extraction from flutter onset time measurements.

During flutter tests, the stagnation pressure is continuously increased at a fixed Mach number in the pressurized wind tunnel until flutter is observed. The safety system is automatically triggered when predefined thresholds are overshot on monitored sensors. A typical flutter onset time data is shown in Figure 6 and clearly illustrates the amplified oscillations endured by the mock-up due to the undamped nature characterizing the flutter phenomenon. The undamped part of the accelerometers and pressure sensors time responses $s(t)$ is isolated and fitted with the analytical function mentioned in equation (4). As the response is analyzed over a few seconds, the curve fit is a good way to cancel out the noise in the raw data. The extracted flutter data are the flutter mode pulsation ω, the flutter (negative) damping ξ and the amplitude and phase of the processed quantity A and φ.

$$s(t) = A \cdot \mathrm{e}^{-\xi \cdot \omega \cdot \mathrm{t}} \cdot \sin(\omega \cdot \mathrm{t} + \varphi) \tag{4}$$

The flutter frequency and damping obtained for each sensor are compared and an average value over many sensors is computed to get a reliable estimate for these flutter characteristics. Finally the curve fit is applied once again but this time the averaged flutter frequency and damping values are imposed in order to get the complex amplitude $A \cdot \mathrm{e}^{\mathrm{i}\varphi}$ of each sensor. In the end, the flutter mode shape can be plotted thanks to the accelerometer data and the flutter mode pressure is available from the pressure sensor data as illustrated in the right part of Figure 6.

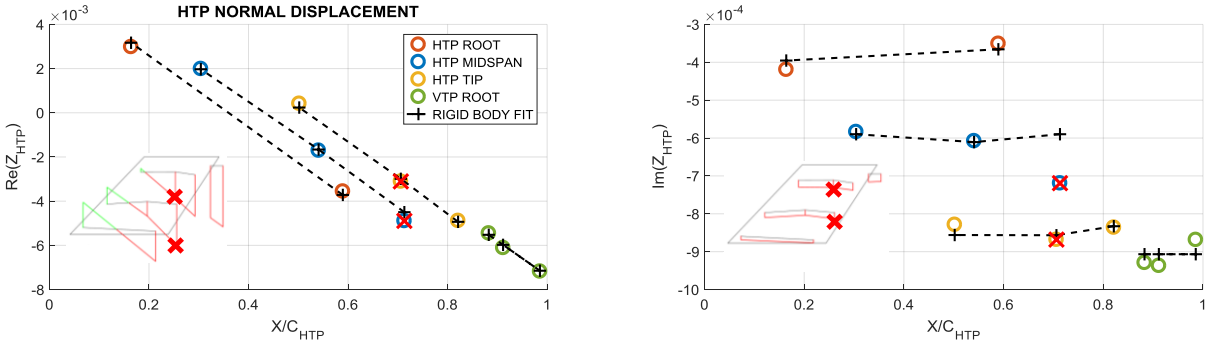

Figure 7: Flutter mode shape obtained with rigid body normalization.

Similarly to the pressure tests data, it is necessary to normalize the flutter tests data in order to know how to compare them with numerical data. Extracted flutter data can be thought of as harmonic data at the flutter frequency with a complex amplitude of $H_{raw}(\omega) = A \cdot \mathrm{e}^{\mathrm{i}\varphi}$ so the rigid body normalization described in the previous section is also applied on these data. Figure 7 gives a good understanding of what happens to the complex flutter shape through the rigid body normalization, namely that the pitching motion is deported exclusively on the real part leaving the other motions composing the flutter mechanism on the imaginary part. Therefore, the rigid body normalization is also suited for the complex flutter mode shape.

2.3 Aerodynamic and flutter computations

This section describes the computational strategy followed to obtain numerical results that can be compared to experimental results. In particular, it points out the great advantage of using a linearized aerodynamic database to obtain easily the flutter mode pressure once the flutter mode shape is available.

2.3.1 CFD mesh & AETHER solver

The CAD model of a U-tail configuration and its associated CFD surface mesh are presented in Figure 8. The surface mesh has 115 400 nodes and 230 200 triangles and the unstructured 3D mesh comprises 10.9 million nodes and 64.9 million tetrahedral. This mesh has been refined in the corner region where the tail surfaces intersect due to the need for corner flow characterization.

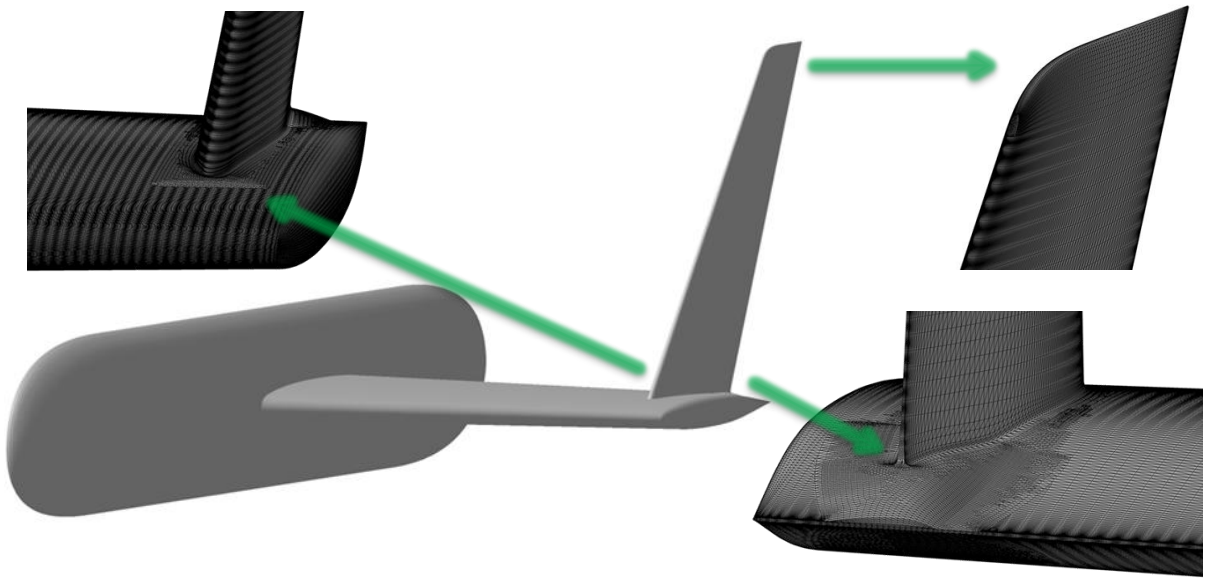

Figure 8: CAD model and CFD surface mesh of a U-tail configuration.

Steady nonlinear computations have been performed with Navier-Stokes RANS model implemented in the in-house flow solver AETHER. Unsteady pressure sensitivities have also been computed with AETHER using a frequency domain linearized Navier-Stokes solver with linearized turbulence. The turbulence modelling is achieved through the Spalart-Allmaras model. More information on AETHER solver is available in [3].

2.3.2 Flutter mode pressure computation

Flutter is governed by equation (5) which is expressed in a modal basis and written in the Laplace domain using the Laplace variable p. In this equation M, C, K are respectively the modal mass, damping and stiffness matrices, GAF is the generalized aerodynamic force matrix, $\mathrm{q_{dyn}}$ is the dynamic pressure, M is the Mach number, k is the reduced frequency, and X is the modal coordinate vector. A linearized pressure data base has been computed by using the structural FEM modes as input for unsteady computations with AETHER solver. This database contains the aerodynamic pressure fields CP_m computed for each FEM mode shape ϕ_m for a range of Mach numbers and reduced frequencies. The GAF matrix is then computed in the ELFINI aeroelastic solver and the flutter equation can be solved, for example, by means of the p-k method.

$$\left[p^2 \cdot \mathrm{M} + \mathrm{p} \cdot \mathrm{C} + \mathrm{K} - \mathrm{q_{dyn}} \cdot \mathrm{GAF}(M,k)\right] \cdot \mathrm{X}(p) = 0 \qquad (5)$$

Several data can be analyzed from flutter computations and compared with experimental data. Numerical flutter curves can be plotted to assess the flutter behavior of the mock-up and can be compared to the experimental ones and the computed flutter pressure can be compared to the measured one during flutter onset tests (see 4.1). Then the computed flutter mode shape

can be retrieved from the flutter computations and can be compared to the measured flutter mode shape (see 4.2). The analysis of the flutter mode is essential since it gives the flutter mechanism, i.e. the combination of the modes involved in the flutter. The final task is to compute the flutter mode pressure field to be compared to the measured one which is available thanks to the flutter onset data extraction method described in 2.2.2.

The flutter mode shape ϕ_{flut} is a linear combination of the ground mode shapes ϕ_m with complex coefficients (or modal coordinates) x_m as expressed in equation (6).

$$\phi_{flut} = \sum_m x_m \cdot \phi_m \tag{6}$$

As linearized Navier-Stokes computations are performed to get the modal pressure field, it is possible to perform linear combinations of the linearized pressure data in order to compute the pressure field corresponding to a combination of modal shapes. Thus, the flutter mode pressure field can simply be obtained by linear combinations of the available modal pressure fields using the flutter mode shape modal coordinates x_m as suggested in (7). This computation should be performed at the flutter mode reduced frequency and the computed flutter mode should be normalized with the rigid body normalization presented in 2.2.1.

$$\mathrm{CP}_{flut} = \sum_m x_m \cdot CP_m \quad \text{where} \quad CP_m = \frac{\partial CP}{\partial \phi_m} \tag{7}$$

As it will be seen, the studied flutter mode is a combination of a pitching motion ϕ_{pitch} and a rolling motion ϕ_{roll}. It is possible to push even further the analysis of the flutter mode pressure field by separating the contribution from the real shape and the one from the imaginary shape. This is simply performed by noticing that $\phi_{pitch} = \sum_m Re(x_m) \cdot \phi_m$ and $\phi_{roll} = \sum_m Im(x_m) \cdot \phi_m$. Hence the pressure fields due to the real and imaginary parts are computed as written in equations (8). The analysis of this decomposition is presented in 4.4.

$$\begin{aligned} \mathrm{CP}_{pitch} &= \sum_m Re(x_m) \cdot CP_m \\ \mathrm{CP}_{roll} &= \sum_m Im(x_m) \cdot CP_m \end{aligned} \tag{8}$$

As one can notice, only CP_m data intervene in equations (7) and (8) and these pressure data are available from the beginning to perform the flutter computations. Hence, working with a linearized pressure database is thus very convenient and an efficient way to perform post-processing analysis without having to perform any additional CFD computations.

3 HARMONIC PRESSURE CORRELATIONS

Harmonic pressure correlations are shown in this section. Steady flow field correlations are presented at first. Secondly, the effect of experimental data normalization on the unsteady pressure correlations is presented. Finally, the applied pitching motion during pressure tests is compared to the theoretical one before analyzing unsteady pressure correlations between experimental results and results from linearized Navier-Stokes CFD computations.

3.1 Steady pressure correlations

In the studied configuration without dihedral and with -2° yaw angle, the mock-up does not deform significantly and the maximum deflection measured by MDM is lower than 0.5 mm at the VTP (Vertical Tail Plane) tip for studied Mach numbers. Hence the static deformed shape has not been taken into account in the steady Navier-Stokes RANS predictions computed with

AETHER solver. Steady pressure coefficients are presented in Figure 9 for three cuts located at the VTP midspan (upper plots), the VTP root (middle plots) and the HTP midspan (lower plots). The pressure coefficient and the boundary layer shape factor (Hi) over the surface are also shown for the VTP outer and inner surfaces in order to give a clear sight of the aerodynamic behavior.

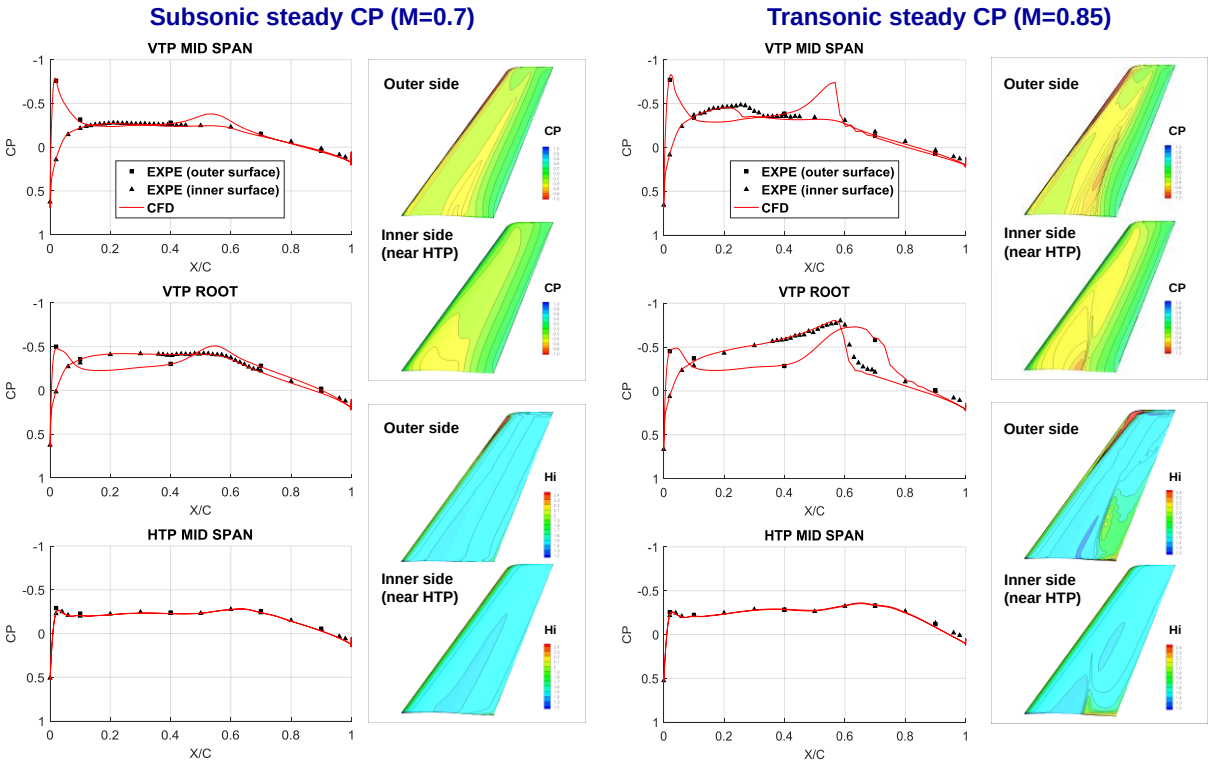

Figure 9: Steady pressure coefficients correlations for subsonic (left) and transonic (right) Mach numbers.

An excellent agreement between measured and computed pressure profiles is observed for both subsonic and transonic Mach numbers. The computed subsonic pressure field is perfectly correlated with the measured CP even in the corner region at the VTP root where the aerodynamic interaction between the surfaces is predominant. At Mach number 0.85, a shock wave appears on both sides of the VTP. It is common to see a shock wave on the outer side of the VTP at such high Mach number, however it should be noted that the shock wave on the inner side (the one facing the HTP) is due to the interaction with the HTP. Thanks to the pressure sensors density on the inner side (triangle markers), it is possible to assess the shock location and amplitude with great accuracy and a very good shock prediction is obtained on this side. The shock location and amplitude on the outer side seems to be well-predicted at the VTP root; however this side is less instrumented (square markers) and no information is available in the shock region at the VTP midspan to assess the CFD prediction. Finally, no flow separation (Hi<2.4) is observed neither experimentally nor computationally in the corner region, however flow separation (Hi>2.4) is observed on the outer side at the VTP tip leading edge and this is confirmed by the measured data (not shown here). These excellent correlations indicate that the steady flow field predictions can be used as input to compute the linearized unsteady pressure sensitivities around these steady states.

3.2 Effect of data normalization

The effect of pressure data normalization is shown in Figure 10 where unsteady pressure profiles are plotted for a cut located at the HTP midspan. The pressure sensitivities induced by

an analytical pitching motion of 1° amplitude around the shaft axis have been computed for two frequencies with the AETHER linearized Navier-Stokes solver (plain black curves). These CFD data are compared with measured pressure data that are normalized with each of the two normalization processes discussed in section 2.2.1. The angular sensor normalization (red markers), which is not appropriate due to the presence of pitching motion in the imaginary part, has a disastrous effect on the imaginary part (right plots) for both frequencies. A good correlation on the real part is observed at 5 Hz (upper plots) but not at 15 Hz (lower plots). The correlations are much better with the rigid body normalization (black markers) for which the expected imaginary pressure profile is recovered, i.e. a zero-crossing along the pitch axis. The correlation on the real part remains the same at 5 Hz however the correlation is now perfect on the real part at 15 Hz.

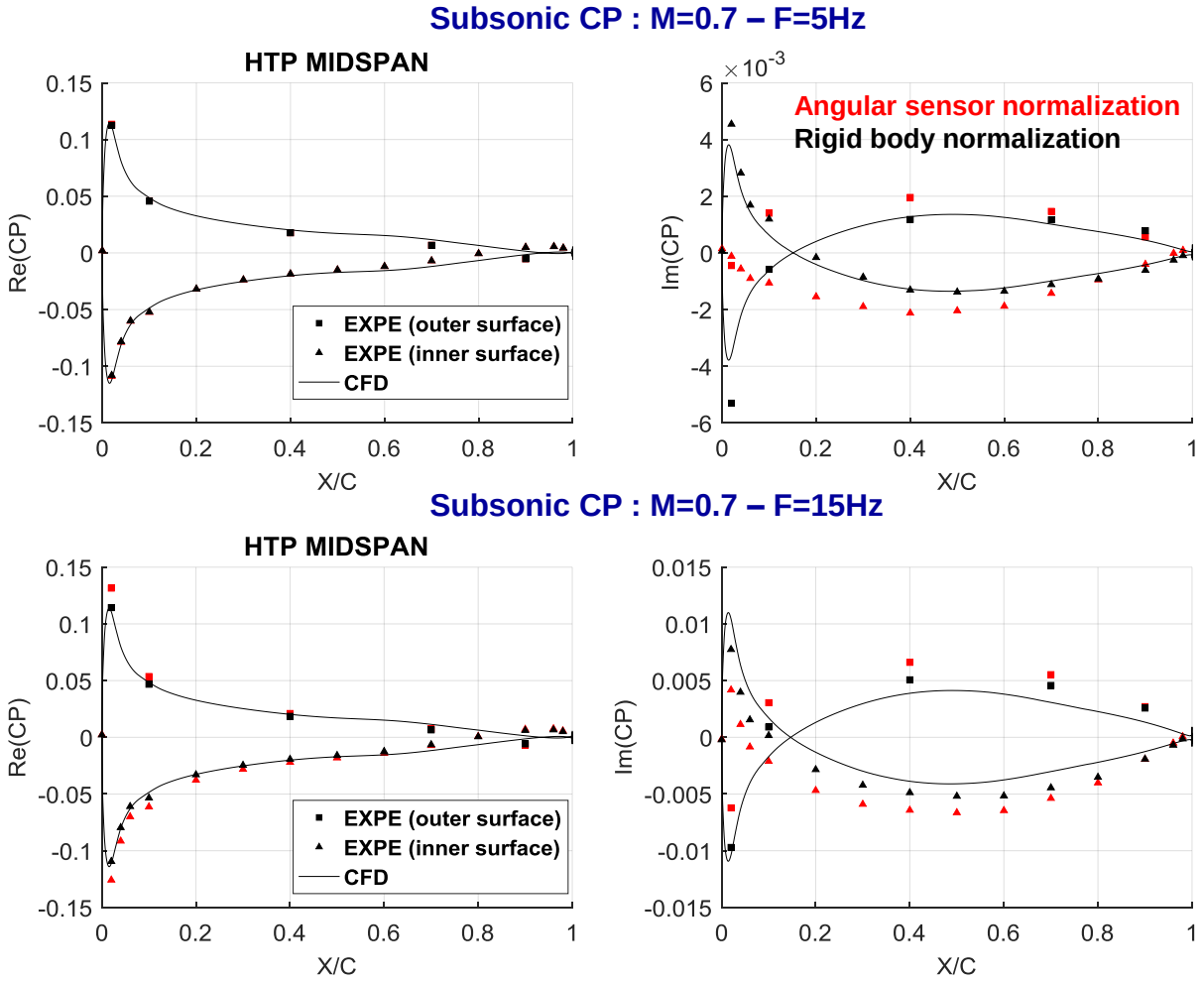

Figure 10: Effect of data normalization on harmonic pressure correlation.

Further investigations have been undertaken to understand why the two data normalizations yield such differences. A phase shift of 2.47° and 2.15° at respectively 5 Hz and 15 Hz has been found between the phase of the angular sensor measurements and the averaged phase of the HTP accelerometer measurements, i.e. the phase of coefficient a in equation (1). Although very small, this phase shift has a tremendous effect on the imaginary part and explains why the imaginary part contains a small part of the pitch shape when data are normalized with respect to the angular sensor. This phase difference may originate from the acquisition system and/or from the dynamic response of the mock-up. Regarding the amplitude, it was found that the angular sensor value is almost 1 at 5 Hz when rigid body normalization is applied,

however its value drops down to 0.87 at 15 Hz. This surprising result explains why the amplitude of the real part is so much different at 15 Hz between the two normalizations while it remains the same at 5 Hz. Once again, measurement issues and mock-up dynamic response may be implicated to explain these differences. In any case, the rigid body normalization is obviously the right one to use if the aerodynamic computations are performed for a 1 degree pitching motion, as it is the case in this article. These investigations show that a small phase shift can have a disastrous impact on unsteady data and that amplitude measurements should always be checked in some way.

3.3 Applied pitching motion

Although harmonic pitch oscillations are imposed thanks to the hydraulic actuator which is connected to the shaft, it is good practice to check if the applied pitching motion corresponds to the believed one i.e. an imposed pitching motion around the shaft axis. In Figure 11, the theoretical pitch shape (red) is superimposed with the measured pitch shape (green) for two frequencies. It appears that the applied shape is almost identical to the expected one for pressure tests performed at 5 Hz, however at 15 Hz the applied shape happens to have an axis (green dotted line) inclined toward the spanwise direction compared to the shaft axis (red dotted line). This qualitative analysis is confirmed by the computation of the measured shape pitch axis which is evaluated during the rigid body normalization process (see 2.2.1). At 5 Hz the measured pitch axis angle is almost equal to the shaft axis angle by 0.4° and is located 10 mm downstream the shaft axis at the HTP root. At 15 Hz the measured pitch axis angle is 6.2° lower than the shaft axis angle, however it crosses the HTP root at the same location. The shift of the line of nodes at 15 Hz can be fully attributed to the dynamic response of the mock-up and could explain why the angular sensor value is not relevant for data normalization as pointed out in the previous section.

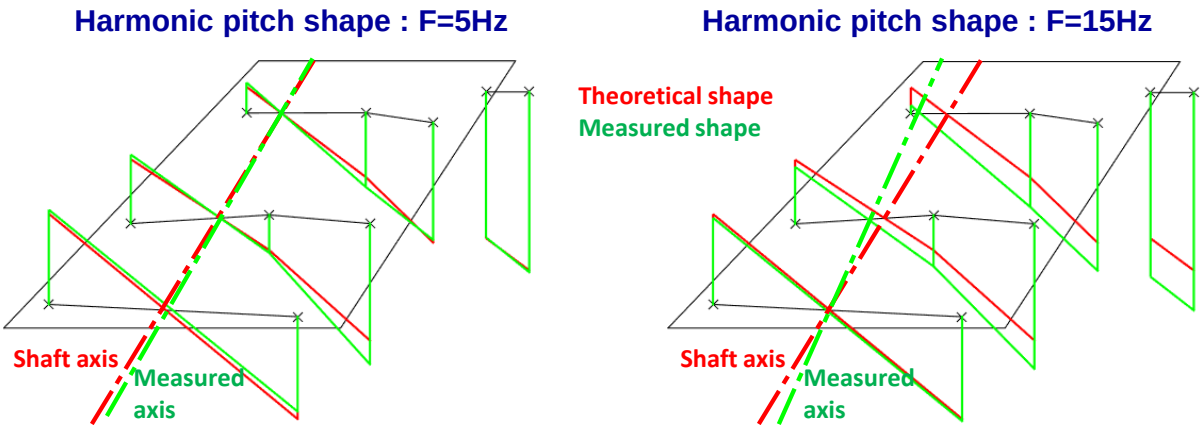

Figure 11: Comparisons of theoretical and measured pitch shapes.

To conclude, the imposed pitching motion corresponds to the applied one at 5 Hz whereas it slightly differs from the expected one at 15 Hz. As a consequence, aerodynamic computations can be performed using the theoretical pitch shape as input at 5 Hz whereas the measured pitch shape should be used as input at 15 Hz. This is true for all the studied Mach numbers.

3.4 Subsonic harmonic pressure correlations

Pressure sensitivities induced by the theoretical pitching motion rotation around the shaft axis have been computed with the linearized Navier-Stokes model coded in AETHER solver. Subsonic pressure profiles are analyzed at three different cut locations for a pitching motion frequency of 5 Hz and 15 Hz in Figure 12 and Figure 13 respectively. On these figures, the

real (left) and imaginary (right) parts of the pressure coefficients are plotted for cuts located at the VTP midspan (upper plots), at the VTP root (middle plots) and at the HTP midspan (lower plots). Measured data have been normalized according to the rigid body normalization and are represented with markers. Triangles are used for "inner" surfaces while square markers are used for "outer" surfaces, where "inner" refers to the fact that surfaces are "inside" the U-shape. Indeed, aerodynamic interactions mainly take place on inner surfaces which is why these sides have been significantly more instrumented with pressure sensors than outer sides.

A very good correlation is obtained at 5 Hz on all the pressure profiles (Figure 12). In particular the real part of the HTP pressure profile agrees very well with the experimental one and the imaginary part is also well predicted with a slight underestimation at the leading edge. On the VTP, the real and imaginary parts of the outer surface are superimposed with measured data at both cut locations. A slight overestimation is noticed on the real part of the inner surface at both cut locations. As for the imaginary part of the VTP inner surface, it is very well predicted at the VTP midspan cut and slightly overestimated in the corner region.

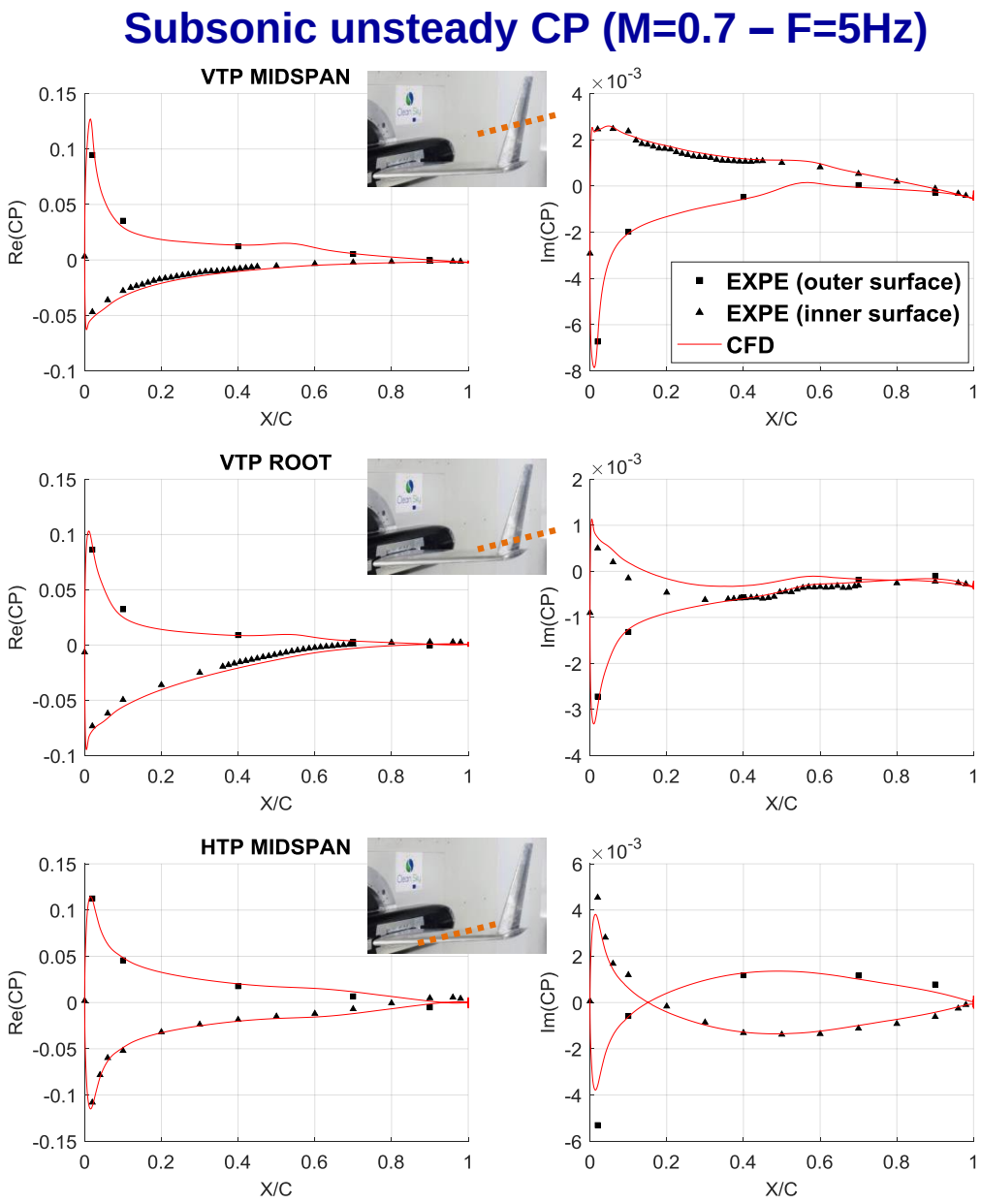

Figure 12: Subsonic harmonic pressure coefficients correlations for an imposed pitching motion at 5 Hz.

The same remarks apply for the real parts at all cut locations at 15 Hz (Figure 13); however the correlation on the imaginary part is slightly degraded. This time, the HTP imaginary part is overestimated at the leading edge while it is underestimated on the rest of the chord. It appears that the zero-crossing is too much backward at 15% chord location while the measured data show a zero-crossing around 10%. This might be due to the fact that the applied pitching motion at 15 Hz is different from the theoretical one (see 3.3). Indeed, the use of the measured pitch shape is likely to shift forward the zero-crossing on the imaginary part. The imaginary parts are slightly overestimated on the VTP at both cut locations. In particular the CFD prediction in the corner differs significantly from the measured imaginary part which drops down; nevertheless a good pressure profile shape is recovered at the VTP midspan. The drop on the imaginary part might be linked to a specific aerodynamic behavior in the corner region and argue in favor of the difficulty to get accurate predictions in this area. These discrepancies are currently not understood and the applied pitching motion should be used to compute the pressures sensitivities at this frequency in order to investigate further on.

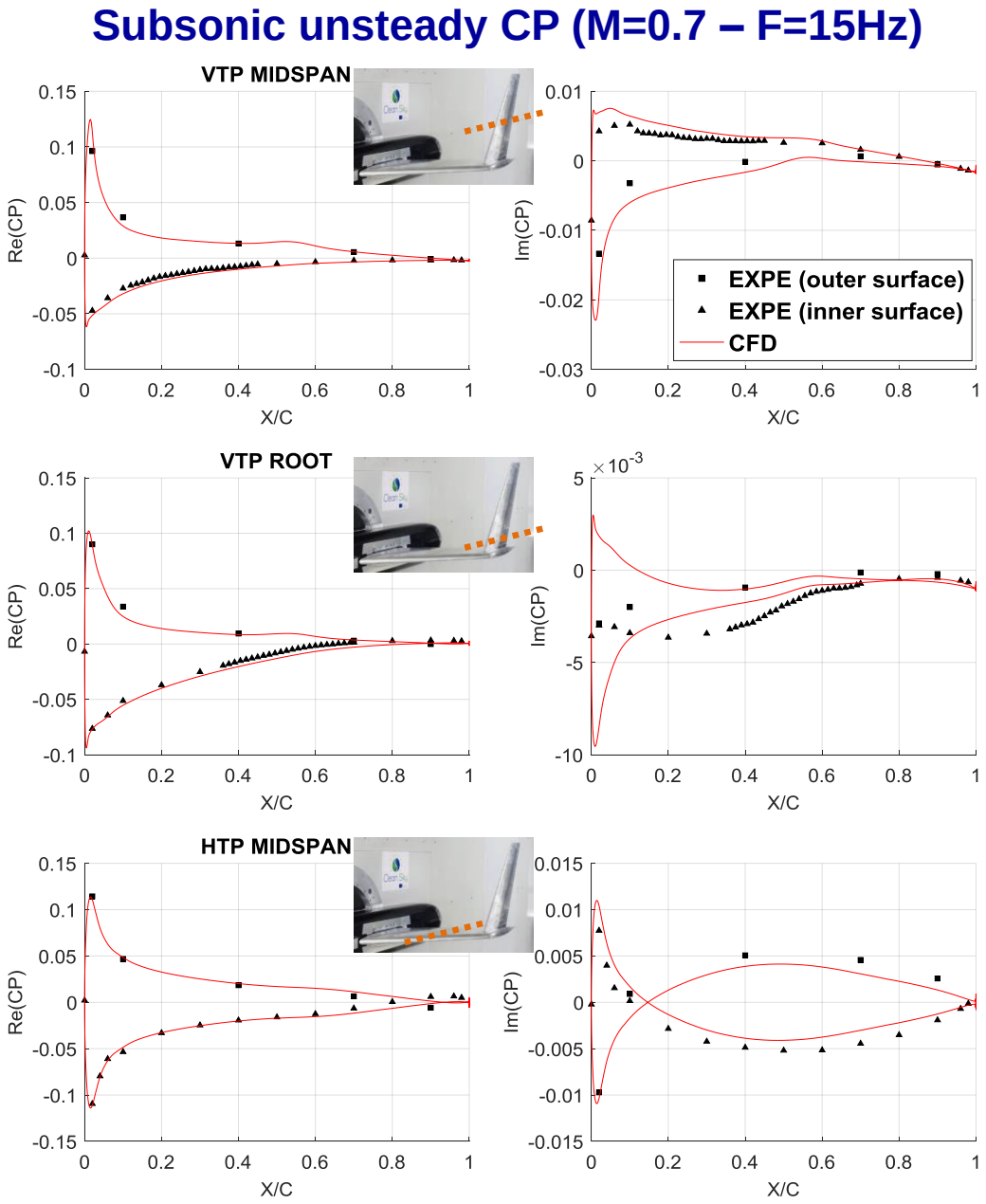

Figure 13: Subsonic harmonic pressure coefficients correlations for an imposed pitching motion at 15 Hz.

Although some discrepancies have been pointed out, the pressure correlations are very satisfactory for this subsonic Mach number. The correlation between the predicted and the measured pressure profiles is slightly degraded on the imaginary part as the frequency increases.

3.5 Transonic harmonic pressure correlations

The analysis presented in the previous section is repeated here below for Mach number 0.85.

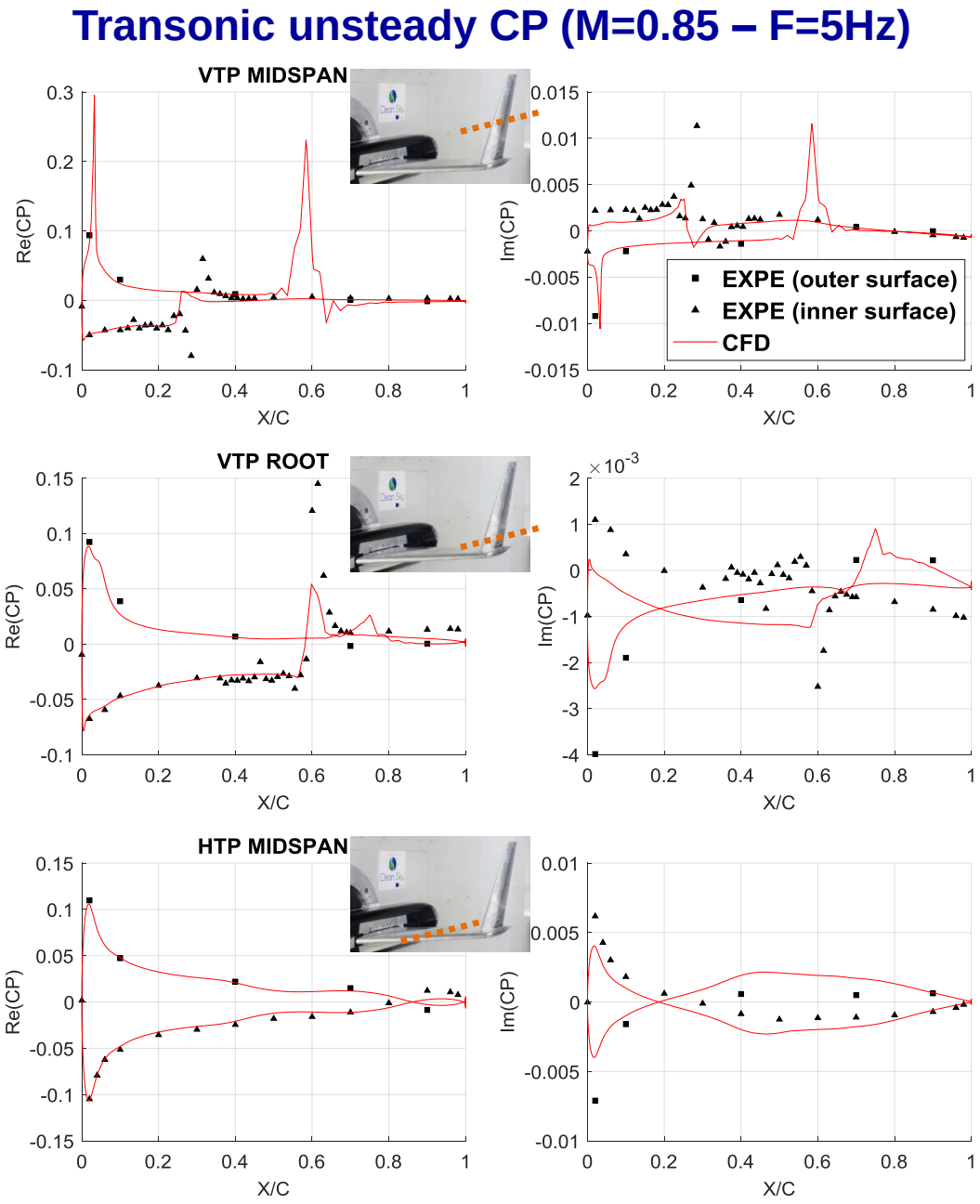

Figure 14: Transonic harmonic pressure coefficients correlations for an imposed pitching motion at 5 Hz.

A good correlation is obtained at 5 Hz on the real part of the pressure profiles (Figure 14). In particular the shock location on the inner surface is well predicted but seems slightly too weak compared to the measurements (triangle markers). A shock is also predicted on the VTP outer surface and seems to be in good agreement with the measured data at the VTP root, however this side is less instrumented (square markers) so it cannot be further analyzed especially at

the VTP midspan where a strong shock is predicted. The predicted HTP pressure profile imaginary part seems to have a zero-crossing upstream of the measured one. The applied pitch shape being identical to the theoretical one, it might be hinted that this is due to flow complexity in the transonic domain. The imaginary part on the VTP seems to be slightly underestimated compared to the measured one particularly in the corner region. However the measured data are quite noisy in this area which might reflect that complex unsteady aerodynamic phenomena take place in the corner region where the HTP and the VTP boundary layers intersect and interact with the shock wave. However these noisy data could also come from measurement issues. Looking at the pressure profile far away from the corner, it can be noticed that the measured data are smoother and that the pressure profile shape is correctly predicted despite the slight underestimation on the VTP inner surface.

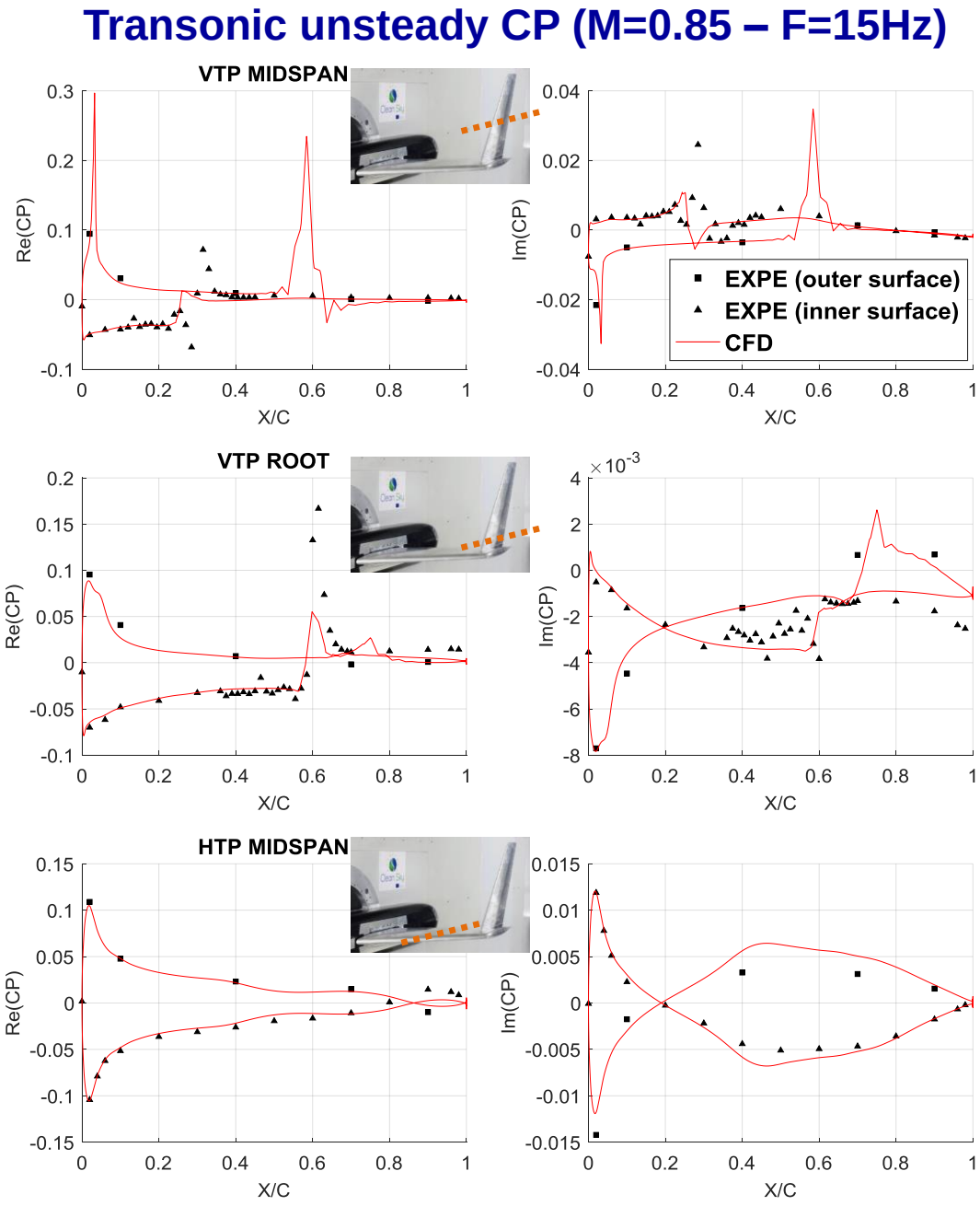

Figure 15: Transonic harmonic pressure coefficients correlations for an imposed pitching motion at 15 Hz.

Surprisingly, the pressure correlations are better at 15 Hz (Figure 15) than at 5 Hz. The same remarks apply for the real part, i.e. good shock location but apparently too weak, but the correlations on the imaginary parts are much better. Firstly the imaginary part on the HTP is almost perfect. Secondly the shape of the imaginary pressure profile in the corner is very similar to the measured one, especially at the leading edge, but the measured data remain noisy around the shock. Finally, the imaginary pressure profile on the VTP midspan is now well-predicted even though the measured shock on the inner surface is slightly backward. As noticed previously for the subsonic Mach number analysis, these computations should be repeated with the applied pitching motion instead of the theoretical one in order to confirm the excellent agreement between numerical and experimental data.

These pressure correlations show that the linearized Navier-Stokes predictions are close to the measured data in the transonic domain. In particular, the shock location is accurately predicted although it seems to be weaker than the measured one on the VTP inner surface. In contrast to the subsonic case, pressure correlations are better at 15 Hz on the imaginary part than at 5 Hz.

4 FLUTTER CORRELATIONS

Flutter correlations in subsonic and transonic domains are presented in this section for a configuration without dihedral and with -2° yaw angle. Firstly, computed flutter curves are compared to the experimental ones. Then flutter mode shape is discussed and the computed flutter mode pressure is compared to the one extracted from flutter onset data. Finally, the contributions of the real and imaginary parts of the flutter mode shape are analyzed in order to get a better understanding of the flutter mode pressure field.

4.1 Flutter diagrams correlations

S2MA Modane being a pressurized wind tunnel, frequency and damping variations can be plotted against the stagnation pressure for a fixed Mach number. Hence flutter diagrams comparisons can be performed Mach by Mach as shown in Figure 16.

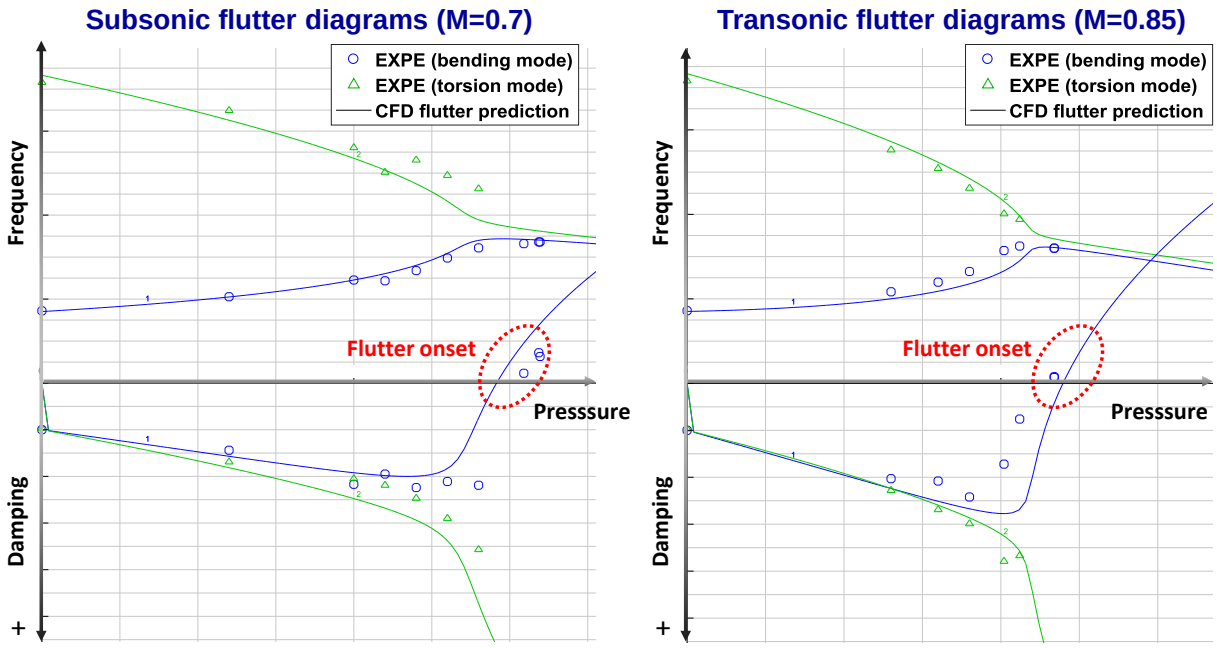

Figure 16: Flutter diagrams correlations for subsonic (left) and transonic (right) Mach numbers.

Good correlations on flutter diagrams are obtained for both Mach numbers. The frequency and damping variations with the stagnation pressure are globally well predicted and the flutter pressure is close to the measured one. At 0.7 Mach number (left plot), excellent correlation is observed on the bending mode curve however the torsion mode frequency variation seems slightly too steep and this mode seems slightly too damped. At 0.85 Mach number (right plot), the torsion mode frequency and damping variations are remarkably well predicted, however the bending mode seems to be slightly overdamped while its frequency variation is too flat.

Unfortunately, it is not straightforward to establish a link between the differences observed on the flutter diagrams and the analysis presented for harmonic pressure correlations. Firstly the ground torsion mode is not a pure pitching motion as it also contains some rolling motion and secondly, modes are coupled in the wind and become complex. Hence each point of a flutter curve corresponds to a complex mode which is a linear combination of ground modes. The last difficulty can be rounded by considering sufficiently low stagnation pressures so that the torsion mode remains mainly itself (low coupling with other modes). Indeed, for low stagnation pressure, the frequency (resp. damping) slope of a mode on a flutter diagram is directly linked to the real part (resp. imaginary part) of the GAF coefficient of the mode which acts as an aerodynamic stiffness (resp. damping) on the mode. This GAF coefficient is the work produced by the aerodynamic field induced by the mode on itself. Consequently, it is possible to relate the frequency and damping slopes to the aerodynamic pressure associated to the mode. As this mock-up has stiff U-tail parts, the rigid pitch imposed in the pressure configuration is close to the pitch contribution in the torsion mode shape so the aerodynamic pressure field due to the pitch motion in the torsion mode is similar to the one measured during harmonic pressure tests. Finally, assuming that a rolling motion induces mainly aerodynamic damping, the torsion mode frequency slope at low stagnation pressures is predominantly related to the real CP due to the pitching motion and its damping slope is related to the imaginary CP due to the pitching and rolling motions.

The slight overestimation noticed on the real CP due to the pitching motion on the VTP inner surface (3.4) could explain why the frequency slope of the torsion mode is too steep for the studied subsonic Mach number. Furthermore, the overestimation of the imaginary CP due to the pitching motion on the VTP could explain why the torsion mode is too damped. As for the transonic Mach number, the predicted real CP is perfectly correlated with the measured one and it appears on the flutter diagram that the predicted frequency slope coincides with the measured one. For the transonic Mach number, no overestimation of the imaginary CP due to the pitching motion has been observed and the damping slope coincides with the measured one. Hence the remarks made on the harmonic pressure correlations seem to be consistent with the slight discrepancies observed on flutter diagrams.

Despite small discrepancies on the flutter curves, the computed flutter diagrams are in very good agreement with the measured ones and the flutter pressure is accurately predicted for both Mach numbers. Indeed, as presented in Figure 17, the predicted flutter pressure variation with respect to the Mach number is very close to the measured one from subsonic to transonic Mach numbers. This demonstrates that the aerodynamic interactions, which have a great influence on the flutter behavior of this mock-up [2], are predicted with a sufficient level of accuracy in regard of the flutter behavior. Thus, linearized Navier-stokes computations give reliable predictions concerning the subsonic and transonic aerodynamic phenomena at stake for this modular U-tail flutter mock-up.

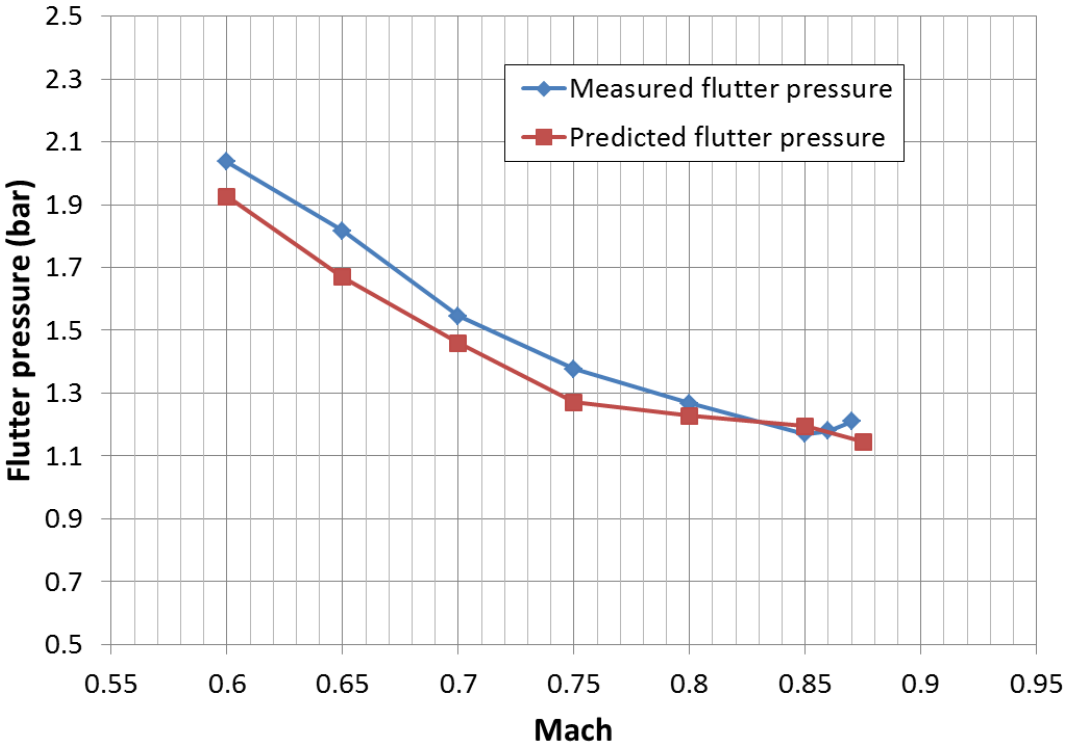

Figure 17: Measured and predicted flutter pressure variations with respect to Mach number.

4.2 Flutter mode shape

Based on the flutter onset measurements, the flutter mode shape has been extracted using the methodology described in section 2.2.2. The measured flutter mode shape is depicted in Figure 18 where the normal displacements of each part of the mock-up are plotted with the following color convention: green for positive and red for negative displacements.

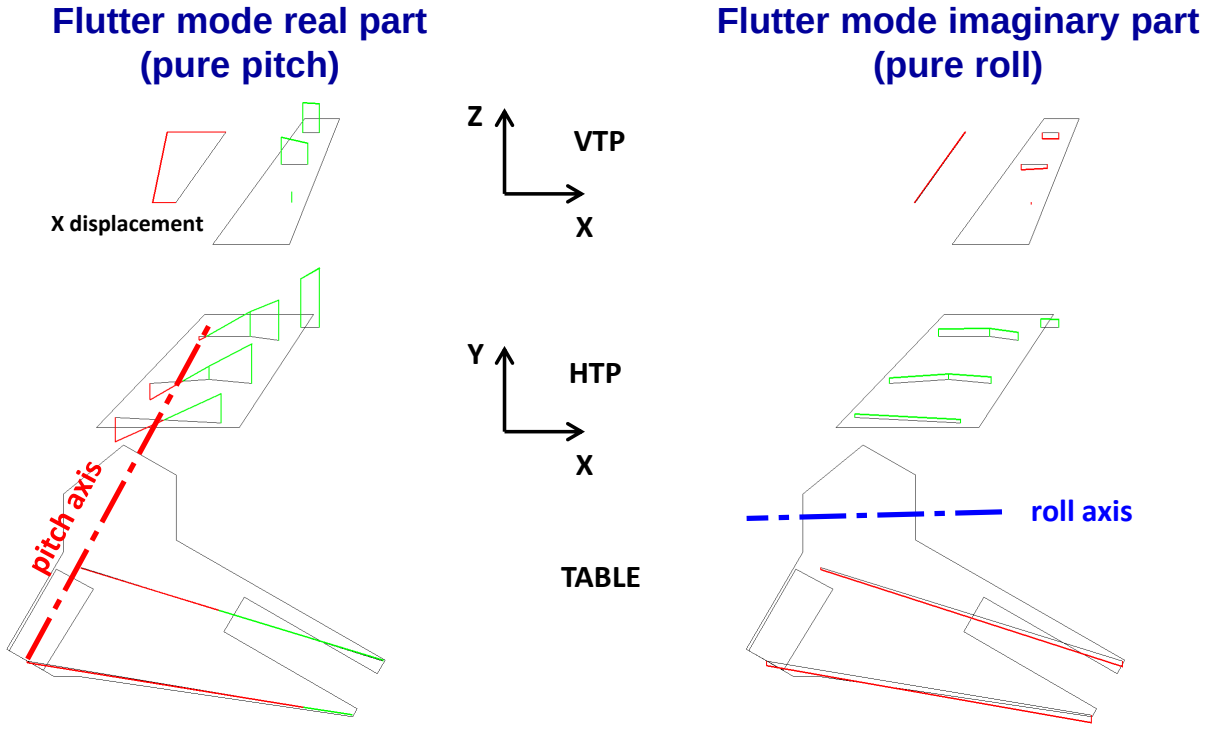

Figure 18: Flutter mode shape extracted from flutter onset measurements.

Thanks to the rigid body normalization, the real part (left) corresponds to a pure pitching motion around a pitch axis (red axis) which is identical to the one depicted on the right picture of Figure 11. The imaginary part corresponds to a pure rolling motion around the roll axis (blue axis). This demonstrates that the flutter behavior of the mock-up corresponds to the targeted bending/torsion mechanism. As seen in the red dotted line circle in Figure 16, three flutter onset tests (blue circle markers) have been performed at Mach number 0.7 and two at Mach number 0.85 (blue circles overlay in the plot). The flutter mode shapes extracted from these five flutter onset measurements are strictly identical, which means that the same flutter mechanism is measured at the studied Mach numbers. The computed flutter mode shape has been compared to the measured one and an excellent correlation is obtained.

4.3 Flutter mode pressure correlations

Flutter mode pressure data have been extracted from the various flutter onset data using the methodology described in section 2.2.2. The computed flutter mode shape has been used to compute the flutter mode pressure field as indicated in 2.3.2. This pressure field can be compared to the extracted one as shown in Figure 19 for Mach number 0.7 (left) and 0.85 (right). These plots are similar to the ones presented previously in 3.4 and 3.5, however this time the analyzed CP correspond to a complex flutter mode shape instead of a real pitch shape. One color per flutter onset is used in Figure 19, hence three sets of markers are plotted for Mach number 0.7 and two for Mach number 0.85. These markers are almost superimposed which highlights, once again, the good repeatability of the measured flutter data and the good structural behavior of the mock-up.

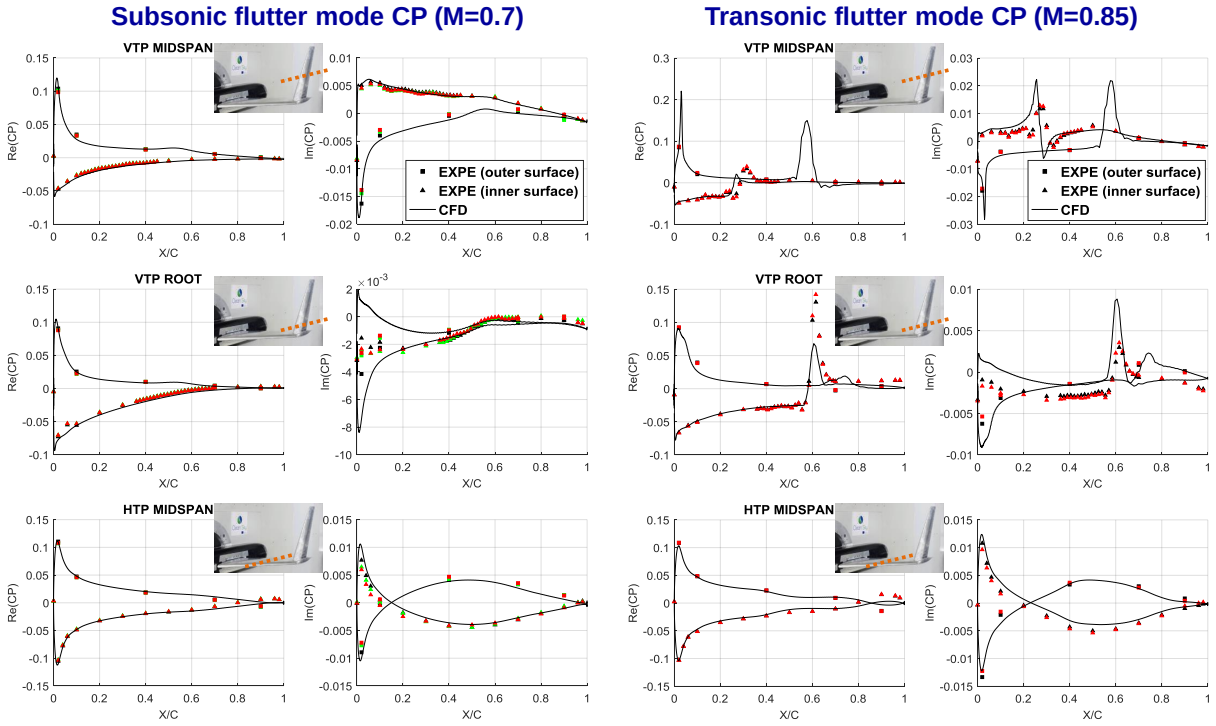

Figure 19: Flutter mode pressure correlations for subsonic (left) and transonic (right) Mach numbers.

Computed pressure coefficients are in excellent agreement with the measured ones at Mach number 0.7, except for the imaginary part at the VTP root (near the corner region). Very good correlations are also obtained for Mach number 0.85 where there is also a discrepancy on the imaginary part at the VTP root. There are slight discrepancies on the other imaginary parts, however the shock location on the VTP inner surface is well predicted and the shock strength

seems underestimated on the real parts while it is overestimated on the imaginary part. It should be noticed that the measured data are remarkably smooth compared to the noisy data shown in 3.5, which is very likely to come from a better signal to noise ratio at flutter onsets than during pressure tests. Indeed, as the mock-up experiences significant oscillation amplitudes due to the diverging nature of the flutter phenomenon, high signal values are recorded which improves the measurement accuracy. Thus, flutter mode pressure analysis is as interesting to analyze as the harmonic pressure tests data and is an additional way to validate the aerodynamic predictions. This is especially true since the flutter mode shape is available and well predicted thanks to the mock-up FEM.

4.4 Flutter mode pressure decomposition

As a linearized frequency-domain approach is used, it is possible to compute the CP contributions of the flutter mode real and imaginary parts without any additional CFD computation (2.3.2). The same results as in Figure 19 are shown in Figure 20 but the CP contribution of the real (red) and imaginary (blue) parts are plotted.

The flutter mode is made of a pitching motion ϕ_{pitch} on the real part and of a rolling motion ϕ_{roll} on the imaginary part (4.2). Hence, on each plot, the total flutter mode CP (black) is thus the sum of pitch contribution and the roll contribution and for clarity the inner surface CP is plotted in straight line while the outer surface CP is plotted in dotted line. This decomposition brings to light that the flutter mode CP is mainly a pitch CP distribution with a minor roll contribution. Furthermore, as the pitch shape of the flutter mode real part is similar to the one applied during harmonic pressure tests, the flutter mode CP comparisons look very similar to the ones presented for the harmonic pressure data. Hence the observations made on harmonic pressure correlations in sections 3.4 and 3.5 are very helpful to understand the discrepancies between the measured flutter CP and the computed ones.

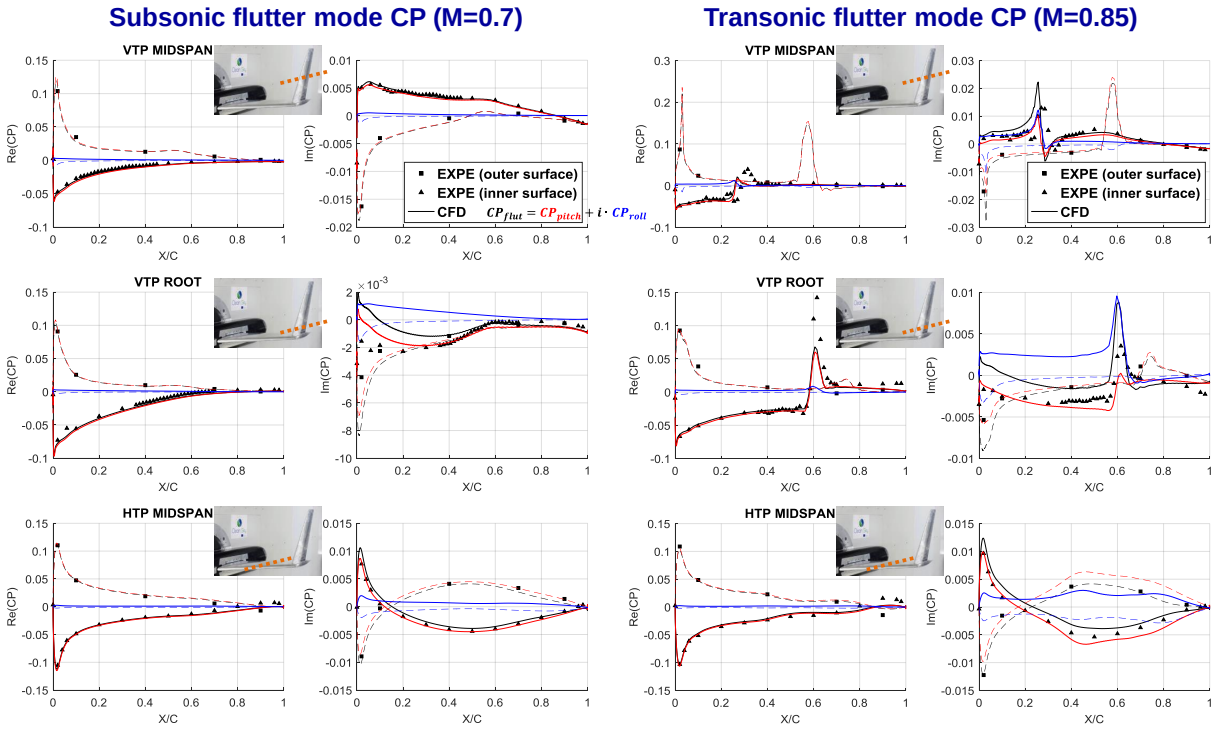

Figure 20: Flutter mode pressure decomposition for subsonic (left) and transonic (right) Mach numbers.

Before discussing the flutter mode pressure decomposition, it is necessary to be aware of the two following facts. Firstly, it should be noticed that thanks to the rigid body normalization, the pitch shape is on the real part. Therefore the real CP (resp. imaginary CP) due to pitch is on the real CP plots (resp imaginary CP plots), and it is no coincidence if the red color has been used to plot the pitch contribution (see Figure 12 to 15). Secondly, the rolling motion is mainly known to produce aerodynamic damping, i.e. imaginary CP, but small aerodynamic stiffness, i.e. small real CP. However, as the rolling motion is on the imaginary part of the flutter shape, the main contribution of the rolling motion should be seen on the real CP plots and a small contribution should be expected on the imaginary CP plots. Based on all these observations, it is possible to draw some conclusions from the flutter mode CP correlations presented in Figure 20.

On the real CP plots, it appears that the roll contribution is derisory compared to the pitch contribution at both Mach numbers. Hence the same observations as the ones made on the harmonic real CP due to pitch apply, namely that excellent correlation is obtained on the HTP for both Mach numbers and on the VTP for the transonic Mach number, however a slight overestimation of the CP is noticed on the VTP inner surface for the subsonic Mach number.

On the imaginary CP plots, it is striking to see that the roll contribution is not as small as one could think about. It is also disturbing to observe that, in the subsonic case, the pitch contribution on its own gives almost perfect correlations with the experimental CP whereas some discrepancies on imaginary CP were observed on harmonic data correlations Figure 13. Two assumptions can be made from these disturbing facts. The first one is that subsonic roll real CP prediction may be overestimated. The second one is that, if this first assumption is validated, the harmonic imaginary CP data might not be as accurate as expected to evaluate the accuracy of unsteady CFD predictions. For the transonic Mach number, similar observations can be made, because although the pitch contribution does not coincide with the measured data away from the leading edge at the HTP midspan and at the VTP root, this was already the case for the harmonic pressure data in Figure 15.

Finally, going back to flutter diagrams correlations, it should be pointed out that the discrepancies observed on frequency variations might also come from the fact that the predicted aerodynamic pressure induced by rolling motion may generate too much aerodynamic stiffness. This assumption has to be further investigated.

5 CONCLUSIONS & PERSPECTIVES

Detailed analyses between experimental and numerical results have been presented based on the pressure and flutter tests performed in ONERA S2MA wind tunnel on a modular U-tail mock-up. Excellent aerodynamic and flutter correlations are obtained both in subsonic and transonic domains which demonstrate that aerodynamic interactions are well predicted by the linearized Navier-Stokes CFD solver AETHER and that frequency-domain flutter computations are suitable to study the flutter behavior of such innovative aft body configurations. A few slight discrepancies between measured and predicted data have been noticed and careful examination of the harmonic pressure correlations together with flutter correlations have revealed possible leads to be further investigated. In the subsonic domain, a small overestimation of the pressure on the VTP inner surface is likely to explain why the torsion mode frequency slope is too steep on the flutter diagrams. In the transonic domain, the shock location is accurately predicted but appears to be weaker than the measured one on the VTP inner surface. Nevertheless, computed flutter diagrams are in very good agreement with the measure ones. For both Mach numbers, the complicated corner flow near the VTP root is

quite well predicted although some discrepancies are observed on the imaginary part; however the measured pitching motion should be used to confirm these observations.

The capability to measure flutter onset data with such a heavy instrumentation and with such good repeatability is very rare and gives access to precious data regarding flutter behavior. Flutter mode shape extraction from measurements allows validating that the computed bending/torsion flutter mechanism corresponds to the measured one and the flutter mode shape is made up of a pitching motion and a rolling motion. Flutter mode pressure data are of excellent quality and appears to be less noisy than harmonic pressure data. This is probably due to the fact that divergent oscillations at flutter onset yield higher amplitudes than the ones applied during pressure tests; thus a better signal to noise ratio is obtained in the measurements. Flutter mode pressure data add up to the harmonic pressure data and are perfectly suited to perform aerodynamic correlations. Similar observations between harmonic and flutter pressure data are obtained thanks to the fact that the imposed pitching motion is almost identical to the real shape of the flutter mode. This is very comforting since flutter and harmonic data have been acquired from two kinds of tests which are very different by nature and are post-processed with completely different techniques. Finally it was noticed that, by decomposing the flutter mode pressure in terms of its real and imaginary shape contributions, the predicted pressure field induced by the rolling motion generates an aerodynamic stiffness which is likely to deteriorate the flutter mode pressure correlations. Hence this aerodynamic behavior should be further investigated.

All the work performed so far to reproduce wind tunnel test measurements leads to excellent aerodynamic and flutter correlations for subsonic and transonic Mach numbers. On the one hand, adequate time measurements post-processing, appropriate data normalization and careful analysis of the experimental conditions are essential aspects that must be thoroughly addressed in order to get reliable experimental results. On the other hand, the capability to take into account experimental conditions in the computations is necessary to obtain numerical results that can be compared to experimental ones. This implies to tune the mock-up FEM with ground vibration tests data to get a representative dynamic behavior and to feed the aerodynamic solvers with measured static and unsteady shapes as input. All these key aspects are integrated in the roadmap followed to perform the experimental and numerical correlations presented in this paper. The excellent correlations obtained in subsonic and transonic domains prove not only that the quality of the experimental database is appropriate for model validation and calibration but also demonstrate that the computational strategy set up at Dassault Aviation to perform aerodynamic and flutter predictions is relevant to assess the flutter behavior of innovative aft body configurations comprising intersecting surfaces. From an industrial point of view, this strategy can be further improved by finding a better compromise between the computational cost of the linearized Navier-Stokes CFD computations and the sufficient level of accuracy admissible to perform reliable flutter predictions.

6 ACKNOWLEDGEMENTS

The research leading to these results has received funding from the European Union's Seventh Framework Programme (FP7/2007-2013) for the Clean Sky Joint Technology Initiative under grant agreement CSJU-GAM-SFWA-2008-001.
This project has received funding from Cleansky-2 Joint Undertaking under the European Union’s Horizon 2020 research and innovation programme under grant agreement N° CS2-AIR-GAM-2014-2015-01.

This paper only reflects the author's view and the CS2 JU is not responsible for any use that may be made of the information it contains.

7 REFERENCES

[1] Geeraert, A., Lepage, A., Stephani, P., Feldmann, D. and Häberli W. (2017). Wind Tunnel Flutter tests of a U-Tail configuration part 1: model design and testing. *IFASD 2017 Conference Proceedings*, IFASD-2017-072.

[2] Mamelle, H., Broux, G. and Garrigues, E. (2017). Wind Tunnel Flutter tests of a U-Tail configuration part 2: Experimental and numerical results. *IFASD 2017 Conference Proceedings*, IFASD-2017-124.

[3] Daumas, L., Forestier, N., Bissuel, A., Broux, G., Chalot, F., Johan, Z. and Mallet, M. (2017). Industrial Frequency-Domain Linearized Navier-Stokes Calculations For Aeroelastic Problems In The Transonic Flow Regime. *IFASD 2017 Conference Proceedings*, IFASD-2017-050.

[4] Garrigues, E. (2018). A Review of Industrial Aeroelasticity Practices at Dassault Aviation for Military Aircraft and Business Jets. *AerospaceLab Journal*, Issue 14 - September 2018.

[5] Colo, L., Broux, G., Garrigues, E. (2019). A New Flutter Prediction Algorithm to Avoid P-K Method Shortcomings. *IFASD 2019 Conference Proceedings*, IFASD-2019-072.

COPYRIGHT STATEMENT